47rd European Rotorcraft Forum
7-10th September 2021
Paper 12

A Propeller Blade Design for Experimental Stall Flutter Investigations

Ross J. Higgins **George N. Barakos**[1]

CFD Laboratory, James Watt School of Engineering, University of Glasgow
Glasgow, G12 8QQ, United Kingdom

Edward Jinks **Nicholas Bown**

Dowty Propellers
Gloucester, GL2 8QN, United Kingdom

With the development of modern propellers for low acoustic emissions and high performance, the influence of propeller aeroelasticity at low speed, highly loaded conditions may induce stall flutter. Therfore, this must be examined to ensure safe operations. To this end, a propeller blade design has been developed which aims to induce torsional stall flutter in a controlled experimental environment. The design has been developed using rigid and elastic CFD, with the results and process presented within this paper. The main objective is to use the final design and test data for validation of CFD and other aeroelastic methods.

1 Introduction

Propeller flutter can manifest in a variety of ways, with the typical phenomena being classical bending-torsion and stall flutter. Classical flutter is driven by the coupling, and excitement, of select structural modes, with such problems, often found due to the structural design and seen within the linear aerodynamic regime[1]. As a result, low-fidelity modelling efforts are available which can obtain the classical flutter boundary via fast calculations[2]. Similarly, stall flutter is driven by the design, but due to the nature of the detached aerodynamics introducing non-linearity, the influence of stall flutter significantly reduces the flutter boundary in comparison to bending-torsion[3]. As a result of this, a deep understanding is required to ensure the safe operation of the propeller.

The development of modern propeller blade designs utilising high twist with sweep, taper and thin aerofoil sections can result in significant changes to the boundary[3, 4]. In addition to this, the development of electric Vertical Take-off/Landing (eVTOL) vehicles is now pushing propellers into significantly different operating conditions[5], further pushing the regime towards potential stall flutter. To this end, an investigation is required to develop a deeper understanding of propeller aeroelasticity and this comes in the form of linked numerical and experimental studies.

[1]Corresponding author, george.barakos@glasgow.ac.uk

To make progress on this research, a new propeller blade design is required for use with the rotor rig of the University of Glasgow[6]. The blade must include the hallmarks of a modern design whilst adhering to the load limits of the experimental rig to be used. To ensure such factors are met, the initial blade design of the wind tunnel rig will be used as a reference.

1.1 Literature Overview

Presented below in Tables 1 and 2 is a summary of the past experimental and numerical studies, respectively, conducted with respect to propeller stall flutter. Greater detail can be found within the PhD thesis, or review paper, of Higgins [3, 4] with a summary discussed below.

In the past, several experimental investigations have been conducted. Due to the heavy use of propeller-driven aircraft between 1945 and 1960, a number of experiments were conducted to understand blade flutter. This included several wooden propeller investigations during the second world war. The use of laminated wood can result in variations in the structural properties during manufacturing and, therefore, such blades remain non-ideal for a numerical simulation. In the 1950s, a range of model blades were designed for wind tunnel investigations. Such blades were made of a modern alloy to allow for a reduction in the variability of the manufacturing process. As a result of this, a range of parameters could be investigated and the greatest insight into stall flutter was found during this period. However, due to the specific design, the blade is not fully defined within the reports and therefore results in non-ideal test cases.

With the aerospace transition from propeller-driven aircraft to turbo-fan engines, interest in propeller stall flutter diminished and therefore very few studies were conducted after the 1950s. A private-sector test was conducted by Dowty Propellers in 1979 using a realistic, in-service blade. Although the primary aim of the test was not specifically for stall flutter understanding, stall flutter was encountered due to the pitch angle range that was used. In addition to this, interest within prop-fans grew in the 1980s and this resulted in new studies to understand the blade flutter boundaries.

With the minimal development in aeroelastic models during the 1950s, interest in numerical stall flutter investigations only began with the development/study of the SR Prop-fans of NASA. These studies, conducted in the 1980s, involved both eigenvalue and time-marching modal methods with semi-empirical aerodynamic models. The use of the eigenvalue analysis was selected to ensure fast calculations and this trend continued into more modern propeller stall flutter studies. With the availability of more computing power, complex finite element models could be used and time-marching analysis was utilised. However, the focus remained on the use of the semi-empirical dynamic stall models and therefore conservative flutter boundaries were achieved [3, 4].

2 Methodology

For this investigation, the CFD solver HMB3 is used to assess the propeller blade design. The core functionality of HMB3 is CFD, however, has been extended in recent years to include whole engineering applications [7, 8, 9, 5, 10]. Previous investigations using HMB3 have provided propeller flow validation in both installed and isolated conditions [11, 12], by comparison with the experimental results of the JORP blade [13], the IMPACTA wind tunnel tests [14, 15] and the model aircraft propeller inflow investigation at the University of Glasgow [16].

To assess the aeroelastic response of the propeller design, two methods are currently available with HMB3. This includes a modal analysis, which was used to investigate stall flutter on the Commander propeller blade [10, 17], and a coupled NASTRAN approach (Middleware), with both methods discussed.

2.1 Modal Aeroelasticity

The modal aeroelastic method uses externally computed structural modes to estimate the structural deformation. This deformation is calculated as the sum of the modal amplitudes for each mode supplied (m), with the modal amplitudes (α_m) calculated based upon the modal equation (Equation 1). The modal equation takes into account the structural damping (ζ_m), mode frequency (ω_m) and modal force (f_m). The modal force is calculated as a projection of the pressure to each of the supplied modes. Further details on this method can be found within the references articles and thesis [10, 17, 3].

$$\frac{\partial^2 \alpha_m^s}{\partial t^2} + 2\zeta_m \omega_m \frac{\partial \alpha_m^s}{\partial t} + \omega_m^2 \alpha_m^s = f_m^s(t) \quad (1)$$

For the previous investigations, a NASTRAN finite element model was created to externally obtain the structural mode shapes and frequencies. The finite element model used non-linear PBEAM elements to model the structural mass and inertia distributions along the blade span with Rigid bar (RBAR) elements used to connect the PBEAM nodes to the fluid mesh points at the given section. A non-linear static analysis (SOL 106) was computed to obtain the mode shapes and frequencies.

2.2 Coupling with NASTRAN

HMB3 is coupled directly with NASTRAN using a communication programme called Middleware. The middleware is a computer code that provides services to applications within the HMB3 tool-set to allow them to exchange data. Figure 1 presents how the communication works when coupling HMB3 with NASTRAN. HMB3 sends the current surface mesh and flow solution to middleware, which processes the data to generate the aerodynamic loads. A call is then used via the purposed operating system to conduct the NASTRAN analysis (typically a non-linear static analysis) and, upon completion, middleware analyses the results files to obtain the node displacements. These are subsequently interpolated onto the CFD surface grid and returned to HMB3 for use in a grid deformation module.

The flexibility of middleware allows for a variety of structural models including one-dimensional beam, two-dimensional plate and a full three-dimensional model. In theory, the beam model used for the modal approach could be used. However, due to the increased flexibility and fidelity, middleware is intended to be used with three-dimensional models (if available).

2.3 Grid Deformation

With both the modal and middleware methods, the structural/grid deformation is handled by HMB3 and, due to the need for flexibility, the process is split into three stages. Firstly, each solid surface is deformed based upon the calculated displacements. These displacements are interpolated between the CSD and CFD grids using a Moving Least Square (MLS) approach. If there are multiple deforming surfaces, the rotation and translation of each solid with respect to the other must be computed and transferred. This is the second stage and it involves the calculation of parent/child shared points, with the deflection matrices computed accordingly. Finally, the effect of the full surface deformation is then implemented in the volume mesh via an inverse distance weighting technique.

The aim of the current work is to utilise both modal and middleware aeroelastic methods. However, for this paper, the focus remains on the derivation of the aerodynamic shape via rigid CFD and its aeroelastic analysis via the modal method.

3 Propeller Blade Design

To ensure the propeller blade design is suitable for use in the desired rotor rig, the rig loads are used as a starting point. This involved the use of the NACA 64-series aerofoil section at the root with a chord of $83.64\ mm$, a twist of 15.56° and an overall radius of $625\ mm$. The remaining aerofoil sections used in the reference blade design were Vertol aerofoils, hence the blade is known as the Vertol blade for this paper. The blade twist, chord, thickness and camber are presented in Figure 2 for the Vertol propeller.

The transition was made to a more propeller-like design via an in-house aerodynamic strip theory code of DOWTY for fast performance estimations. Utilising this and transitioning to NACA 16-series aerofoil sections, the twist, chord and thickness profiles presented in Figure 2 for the NACA blade were derived. This resulted in a reduction in local pitch angle towards the tip, reduction in chord towards the root and tip, and an increase in thickness towards the tip.

Vertol aerofoils are typically used in helicopter blades due to their low camber design and with camber being the most critical factor in the performance of the blade, the decision was taken to adopt the thickness, chord and twist profiles of Dowty and assess to different camber options. A high (named NACA Mrk-12) and low camber (named NACA Mrk-11) blade versions were derived with the profiles presented in Figure 2(a).

3.1 Simulation Setup

To assess the two variants, each design was analysed in isolation via a rigid CFD simulation with the Scale-Adaptive-Simulation (SAS) formulation of the $k-\omega$ SST turbulence model. The SAS formulation is a hybrid RANS/LES model that incorporates an adaptable resolved scale to capture the highly non-linear detached flow aerodynamics [18]. This is an unsteady method, hence the blade is rigidly rotated around its axis in steps of 0.5° .

The test conditions used for the simulations are presented in Table 3. A design inflow of $38\ m/s$ is used at a rotational velocity of $3000\ rpm$. This results in reference Reynolds and Mach numbers of $0.17M$ and 0.11, respectively. The reference pitch angle is set to 32° at $70\%R$. These conditions represent what is expected to be achievable during the wind tunnel investigation.

To match the resolution between each blade design, the same grid topology and node distribution is used in the chimera foreground grid on the blade. Utilising the chimera method allows for a uniform, and constant, background grid to be derived with only changes made to the shape of the blade in the foreground. The definition of the grid and domain is presented in Figure 3. Overall, a foreground grid of 0.9M cells is combined with a 10.4M background to result in a full isolated blade grid of 11.3M cells.

3.2 Rigid SAS Results

Presented in Figure 4 are the blade iso-surfaces of Q-criteria with a value of 0.005 for the Mrk-11 and Mrk-12 blades. Both blades are seen to have tip-dominant stall bubbles with linear attached flow observed up until $75\%R$. The detached flow is seen to fully shed, from both blades, four times per revolution, with the Mrk-11 blade including higher frequencies and secondary stall events during the shedding process.

These secondary events are highlighted within the propeller loads. The overall propeller thrust and blade pitching moment are presented in Figure 5. For reference, steady RANS results using the hover-formulation of HMB3 [19] are also presented to given an indication as to the detached flow effect. Focusing on the propeller thrust results (Figure 5(a)), the average thrust reduces by $\sim 11.7\%$ for both Mrk-11 and Mrk-12 with the use of the SAS model. The higher cambered Mrk-12 blade is seen to oscillate at $\pm 44\ N$ with this driven by the $4\ revolution$ detachment of the tip stall bubble. The Mrk-11 blade oscillates at a lower value of $\pm 39\ N$ and this is influenced by the secondary detached flow events which occur at higher frequencies throughout the revolution.

Both propellers are seen to be well within the thrust limit of the experimental rig. The blade pitching moments, that contribute to the torsional response, are presented in Figure 5(b) for both blades. Overall, both blades experience a significant torsional moment indicating a likely torsional response. The Mrk-12 blade is seen to have a higher magnitude than the Mrk-11, with a difference of 16% between the average SAS results. Additionally, the direction of the rotation switches between the blades with the Mrk-12 having a pitch-up response. This pitch-up response is likely to have a significant influence on the stall flutter boundary by generating higher pitch angles and thus introducing greater levels of detached flow.

3.3 Summary of Findings

It is clear from the rigid CFD results that two distinct paths have formed. For the NACA Mrk-11, a larger amount of stall content at a lower thrust value is present, hence there is a greater scope to vary in terms of the reference pitch angle. Additionally, the pitch-down moment may reduce the overall angle of attack and therefore oscillate the blade in and out of stall. For the NACA Mrk-12, the overall stall volume appears the same, however, the shedding occurs in a much more controlled manner. Greater thrust values are found for this blade but remain within the experimental limits with $\sim 8^{\circ}$ reference pitch remaining to explore. The pitch-up moment will likely induce further detached flow content and overall load.

From this result, the Mrk-11 was chosen to take forward for aeroelastic analysis. The pitch-down moment will likely ensure a safer operation in the wind tunnel and the non-integer load frequencies can indicate during the experimental runs that the blade is approaching the desired conditions via the monitoring of the gauge plots.

4 Aeroelastic Analysis

Following the derivation of the blade aerodynamic design, the focus switched to the understanding of

the blade aeroelastic response. This required the verification of the blade structural design along with the derivation of a beam structural model to transition between the previous modal aeroelastic simulations and the higher fidelity method of Middleware. For this analysis, the reference conditions of the rigid simulations (Table 3) are used. Discussion is now presented on the derivation of the structural models, followed by the aeroelastic results.

4.1 NACA Mrk-11 Structural Model

4.1.1 Full Finite Element Model

As this is a bespoke blade intended for use within the wind tunnel of the University of Glasgow, the full structural model had to be designed. For this, inspiration is taken from the reference Vertol blade with the design including the following components: a rig-mountable root fitting, D-spar beam, rear filler, tip cap and outer aerofoil skin. The intended manufactured blade will include no filler rearward of the beam due to the need to place the strain-gauge wiring, however, it has been included within this model to complete the structure. The tip cap is used to insert ballast for balancing purposes with 10 cylindrical holes included for use across the tip chord length. To ensure the same radial extension of the root fitting into the centre of the blade as the Vertol, an additional reference station was included within the blade planform along with the switch to blunt trailing edges. Hence, the blade was renamed the NACA Mrk-11+. A combination of aluminium, steel and composites are used across the blade.

With the full CAD model defined, attention turned to the derivation of unstructured volume meshes for each components use in Nastran. These were generated using ICEM-Hexa™ of ANSYS. The unstructured meshing allows for the nodes to be defined on the curves of the geometry, with additional settings used to define the minimum size across a surface and desired type of element. This includes tetrahedrons, pyramids, prisms and quadrilaterals. For these grids, tetrahedrons were used due to the easier generation of the volume grid. Presented in Figure 6 is the full volume grids for the NACA Mrk-11+, split open to show each component, with the volume grids sizes presented in Table 4.

To connect each component of the grid, contact bodies are used. These allow for a ”glueing” between components with the glue option selected to ensure no penetration between components. In addition to the merging of components, single point constraints (`SPC1`) are used across the inner most cells of the root fitting in order to clamp the root of the blade in all directions.

One critical factor in the mode shapes and frequencies of the blade is the effect of the blade rotation. To simulate this effect, an `RFORCE` load is applied. The setup requires its inclusion as the non-rotating modal response can always be extracted through an `RFORCE` of zero magnitude.

Due to the combination of these factors, the contact bodes, single point constraints and centrifugal force, the Nastran solution number 400 (SOL 400) is required. This is an implicit non-linear solver that combines the historic methods of SOL 106 with the advancements in grid generation (contact bodes). SOL 400 requires the placement of several steps across a subcase to ensure the effect of the rotational force is carried to the modal analysis. Additionally, a linear solution can be selected, should the case require it. The combination of non-linear/linear and with/without rotation has been compared against a reference modal analysis using SOL 103 to check the solution.

4.1.2 Beam Structural Model

In tandem with the full FEM model, a structural beam model is derived using each of the components of the full FEM with a solid material blade assumed. An estimate for the overall properties was gained via a combination of the included components based upon the respective volume. These respective volumes and the final material properties are presented in Table 5.

With the assumption of a solid material blade, the inertia’s were estimated using the integration of the shape over the area. These were then adjusted to match the non-rotational mode shapes order and frequency of the full FEM. Presented in Figure 7 is the tuned inertias for the NACA Mrk-11+.

4.1.3 Nastran Modal Analysis

Presented in Table 6 is the comparison of the non-rotational mode shapes and frequencies between the beam and full FEM models. The mode shape order is found to be well preserved. However, there are some differences in the derived frequencies, particularly modes 3 and 4. These are greater than

10%, however, are in opposite directions. Therefore, any attempt to adjust the inertias to match a single mode would offset the other and, additionally, the first mode (which is within 2% of the full FEM). Overall, the first response of the flapping, lag and torsional modes are captured in the beam model.

Presented in Figure 8 is the Spoke diagram for the beam and full FEM models. The offset seen in modes 3 and 4 is subsequently carried over to the rotational frequencies. The well-matched modes, i.e. the first flapwise bending, lag bending and torsional modes, mirror the full FEM trend. Although difficult to observe in Figure 8 due to the scales of the frequencies, each mode increases due to the stiffening effect of the rotating blade with changes between 3 and $30\ Hz$. Some of the plots are found to be very close to the engine orders, with a crossing indicating a potential resonance, however, no resonances are found for either the beam or full FEM model at the baseline velocity of $3000\ rpm$.

4.2 Simulation Setup

With a starting aerodynamic solution derived from the rigid SAS computations, the aeroelastic computations can simply be restarted from this point. As previously discussed, the modal aeroelastic method requires the supply of the mode shapes and frequencies for the blade. For this, the beam model was used in the supply of these with the supplied modes presented in Table 7. These frequencies take into account the effect of the simulated centrifugal force at $3000\ rpm$. In addition to the dynamic response, the static displacement due to the rigid aerodynamic loads and the centrifugal force is included.

4.3 Aeroelastic Results

Presented in Figure 9 is the modal amplitude and force results for the aeroelastic blade. Focusing on the modal amplitudes in Figure 9(a), the greatest amplitude magnitude is found in mode 1 with an average value of -5.53×10^{-7}. This compares to the average values of 4.83×10^{-9}, -2.46×10^{-8}, -4.67×10^{-9}, and -6.74×10^{-9} for modes 2, 3, 4 and 5, respectively. Taking the percentages of these averages with respect to mode 1 results in values of 0.9%, 4.4%, 0.9%, and 1.2%, respectively. This indicates that although the majority of the blade deflection is governed by mode 1, an influence may be felt by the second flapwise and first torsional modes. Often the fluctuation across the average can give an indication of potential stall flutter with percentage values, with respect to the average, of 5.6%, 30.4%, 8.0%, 6.6% and 7.7% seen for modes 1, 2, 3, 4, and 5, respectively. This indicates that the lagwise bending mode is more influenced by the fluctuations in loads, despite having the lowest average value. In terms of raw values, the fluctuations in mode 1 still dominate over all other modes.

The modal forces are presented in Figure 9(b), with these values effecting the overall amplitude response of Figure 9(a). As expected, mode 1 has the highest magnitude with an average value of 0.45. However, unlike the modal amplitudes, the force values for mode 5 follows closely in magnitude to mode 1 with an average value of 0.43. This is then followed by modes 4, 3 and 2 with averages of 0.29, 0.29 and 0.03, respectively. This would suggest that the torsional mode (mode 5) has a significant effect on the overall amplitude. However, the large force combined with the high frequency results in a reduced amplitude effect. With very little effect found in terms of the change in mode shape with an inertia adjustment to trim mode frequencies, a significant reduction in this frequency could result in the active mode switching from the first flapwise bending to the first torsion.

Presented in Figure 10 is the blade deformation in terms of bending and twist. Both bending and twist results follow a fairly similar, stable profile, indicating the domination of the static deflection. The maximum deflection is seen towards the tip with only minor fluctuations across the examined revolutions. In terms of maximum values, the blade is seen to bend by $22\ mm$ and twist by 0.16° . These are very low values and are driven by the small modal amplitude values presented in Figure 9.

Due to the relatively stable deformation of the Mrk-11+ blade, the loads remain fairly consistant with respect to the rigid values. The overall propeller blade loads are presented in Figure 11 and show the overall propeller thrust and torque. Although positive with respect to the experimental rig limits, the lack of elastic fluctuation indicates that the current aeroelastic changes have no significant effect on the aerodynamics.

5 Conclusion and Future Work

To conclude, a propeller blade design aimed for use within a wind tunnel environment has been studied in a rigid and elastic manner using CFD. Both the rigid and elastic results indicate the presence of stall via the flow-field visualisations and load oscillations. The stall appears concentrated towards the tip of the blade. However, based upon the current modal aeroelastic analysis, the blade deflections are kept fairly minimal due to the high frequencies associated with the structural model. Further analysis is required in terms of aeroelastic setup and potential future tuning for the desired aeroelastic effect. This includes tuning of the structural model for lower excitation of the torsional modes or tuning of the conditions for excitation of specific modes. As well as the option of refining the operating conditions to provide even larger variations in aerodynamic twisting moment in attempt to trigger greater variations in local, sectional incidence and therefore larger amplitude force oscillations.

Acknowledgements

The support provided by Dowty Propellers for the project NESPA is greatfully acknowledged.

References

[1] Wright, J. and Cooper, J., *Introduction to Aircraft Aeroelasticity and Loads*, John Wiley & Sons, Ltd., 2nd ed., 2015.

[2] Hodges, D. and Pierce, G., *Introduction to Structural Dynamics and Aeroelasticity*, Cambridge University Press, 2011.

[3] Higgins, R., *Investigation of Propeller Stall Flutter*, Ph.D. thesis, University of Glasgow, 2020.

[4] Higgins, R., Barakos, G., and Filippone, A., "A review of propeller stall flutter," *The Aeronautical Journal*, 2021, Submitted for publication.

[5] Higgins, R., Barakos, G., Shahpar, S., and Tristanto, I., "A Computational Fluid Dynamic Acoustic Investigation of a Tiltwing eVTOL Concept Aircraft," *Aerospace Science & Technology*, Vol. 111, 2021, DOI: 10.1016/j.ast.2021.106571.

[6] "MENtOR: Methods and Experiments for NOvel Rotorcraft," gtr.ukri.org/projects?ref=EP/S013814/1, 2021, Last accessed 9^{th} June 2021.

[7] Dehaeze, F. and Barakos, G., "Mesh deformation method for rotor flows," *Journal of Aircraft*, Vol. 49, No. 1, 2012, pp. 82–92, DOI: 10.2514/1.C031251.

[8] Chirico, G., Barakos, G., and Bown, N., "Numerical aeroacoustic analysis of propeller designs," *The Aeronautical Journal*, Vol. 122, No. 1248, 2018, pp. 283–315, DOI: 10.1017/aer.2017.123.

[9] Crozon, C., Steijl, R., and Barakos, G., "Coupled flight dynamics and CFD - demonstration for helicopters in shipborne environment," *The Aeronautical Journal*, Vol. 122, No. 1247, 2018, pp. 42–82, DOI: 10.1017/aer.2017.112.

[10] Higgins, R., Jimenez-Garcia, A., Barakos, G., and Bown, N., "High-Fidelity Computational Fluid Dynamics Methods for the Simulation of Propeller Stall Flutter," *AIAA Journal*, Vol. 57, No. 12, 2019, DOI: 10.2514/1.J058463.

[11] Barakos, G. and Johnson, C., "Acoustic comparison of propellers," *International Journal of Aeroacoustics*, Vol. 15, No. 6-7, 2016, pp. 575–594, DOI: 10.1177/1475472X16659214.

[12] Higgins, R., Zarev, A., Barakos, G., and Green, R., "Numerical Investigation of a Two-Bladed Propeller Inflow at Yaw," *Journal of Aircraft*, Vol. 57, No. 2, 2020, DOI: 10.2514/1.C035647.

[13] Scrase, N. and Maina, M., "The Evaluation of Propeller Aero-acoustic Design Methods by Means of Scaled-Model Testing Employing Pressure Tapped Blades and Spinner," *19th ICAS Congress, Anaheim, California, USA.*, International Council of the Aeronautical Sciences, 1994, ISBN: 1563470845.

[14] Gomariz-Sancha, A., Maina, M., and Peace, A., "Analysis of propeller-airframe interaction effects through a combined numerical simulation and wind-tunnel testing approach," *53rd AIAA Aerospace Sciences Meeting*, AIAA, Kissimmee, Florida, 2015, DOI: 10.2514/6.2015-1026.

[15] Knepper, A. and Bown, N., "IMPACTA Windtunnel Instrumentation Specification," Tech. Rep. ITS 01777, Issue 3, Dowty Propellers (GE Aviation Systems Ltd), 2014.

[16] Zarev, A. and Green, R., "Experimental investigation of the effect of yaw angle on the inflow of a two-bladed propeller," *Aerospace Science and Technology*, Vol. 103, 2020, pp. 105940, DOI: 10.1016/j.ast.2020.105940.

[17] Higgins, R., Barakos, G., and Jinks, E., "Estimation of Three-Dimensional Aerodynamic Damping using CFD," *The Aeronautical Journal*, Vol. 124, No. 1271, 2019, pp. 24–43, DOI: 10.1017/aer.2019.135.

[18] Menter, F. and Egorov, Y., "The Scale-Adaptive Simulation Method for Unsteady Turbulent Flow Predictions. Part 1: Theory and Model Description," *Flow, Turbulence and Combustion*, Vol. 85, No. 1, 2010, pp. 113–138, DOI: 10.1007/s10494-010-9264-5.

[19] Steijl, R., Barakos, G., and Badcock, K., "A framework for CFD analysis of helicopter rotors in hover and forward flight," *International Journal for Numerical Methods in Fluids*, Vol. 51, No. 8, 2006, DOI: 10.1002/fld.1086.

[20] Sterne, L., "Spinning Tests on Fluttering Propellers," *Aeronautical Research Council: Reports and Memoranda*, , No. 2022, 1945.

[21] Theodorsen, T. and Regier, A., "Effect of lift coefficient on propeller flutter," Tech. Rep. L5F30, National Advisory Commitee for Aeronautics, 1945.

[22] Ewing, H., Kettlewell, J., and Gaukroger, D., "Comparative flutter tests on two, three, four and five-blade propellers," Tech. Rep. 2634, Aeronautical Research Council, 1952.

[23] Baker, J., "The effects of various parameters, including Mach number, on propeller-blade flutter with emphasis on stall flutter," Tech. rep., National Advisory Commitee for Aeronautics, 1955.

[24] Hubbard, H., Burges, M., and Sylvester, M., "Flutter of thin propeller blades, including effects of Mach number, structural damping, and vibratory-stress measurements near the flutter boundaries," Tech. Rep. 3707, National Advisory Commitee for Aeronautics, 1956.

[25] Allis, A. and Swihart, J., "THE EFFECT OF BLADE-SECTION CAMBER ON THE STALL-FLUTTER CHARACTERISTICS OF THREE NACA PROPELLERS AT ZERO ADVANCE," Research Memorandum L53B17, National Advisory Committee for Aeronautics, 1956.

[26] Rogallo, V. and Yaggy, P., "A wind-tunnel investigation of the stall-flutter characteristics of a supersonic-type propeller at positive and negative thrust," Technical Memorandum 3-9-59A, National Aeronautics and Space Administration, 1959.

[27] Burton, P., "Straingauge Test Report on a Spin Test Carried out on a Type (c) R.305/3-82-F/6 Propeller on the Spinning Tower at the R.A.E. Farnborough, Hants." Tech. Rep. 093.1.592, DOWTY ROTOL LTD., 1979.

[28] Smith, A., "Analysis and Test Evaluation of the Dynamic Stability of Three Advanced Turboprop Models at Zero Forward Speeds," Contractor Report 175025, National Aeronautics and Space Administration, 1985.

[29] Smith, A., "Analysis and Test Evaluation of the Dynamic Response and Stability of Three Advanced Turboprop Models at Low Forward Speeds," Contractor Report 175026, National Aeronautics and Space Administration, 1985.

[30] Bielawa, R., Johnson, S., Chi, R., and Gangwani, S., "Aeroelastic Analysis for Propellers: Mathematical Formulations and Program User's Manual," Contractor Report 3729, National Aeronautics and Space Administration, 1983.

[31] Reddy, T. and Kaza, K., "Analysis of an unswept propfan blade with a semiempirical dynamic stall model," Tech. rep., National Aeronautics and Space Administration, 1989.

[32] Delamore-Sutcliffe, D., *Modelling of Unsteady Stall Aerodynamics and Prediction of Stall Flutter Boundaries for Wings and Propellers*, Ph.D. thesis, University of Bristol, 2007.

[33] Ognev, V. and Rosen, A., "Influence of using various unsteady aerodynamic models on propeller flutter prediction," *Journal of Aircraft*, 2011.

Table 1: Summary of propeller stall flutter experimental test cases.

Test Case	Pros	Cons	Conditions
Spitfire/Firefly Propellers [20]	*1:* Clear stall flutter boundary *2:* Known geometry	*1:* Wooden blade *2:* Structural properties	*rpm:* $800 - 1800$ *Pitch:* $8^\circ \ -32^\circ$
Theodorsen Models [21]	*1:* Clear stall flutter boundary	*1:* Wooden blade *2:* Blade definition *3:* Experimental setup	*Non-dimensionalised*
Tempest Propeller [22]	*1:* First non-wooden blade *2:* Stress traces across range	*1:* Coarse pitch range *2:* Multi-blade setup *3:* Blade definition	*rpm:* $900 - 1600$ *Pitch:* 12, 16, 20, 24, 28, 30°
Baker/Hubbard Models [23, 24]	*1:* Dimensionless boundary *2:* Extensively analysed	*1:* Structural properties *2:* Non-realistic blades (model only)	*Pitch:* $5^\circ \ -35^\circ$
NACA Propellers [25]	*1:* Extensively analysed *2:* Blades defined	*1:* Experimental setup *2:* Blade trim	*Pitch:* $16^\circ \ -38^\circ$ *rpm:* $\sim 400 - 1700$
Rogallo Models [26]	*1:* Extensively analysed *2:* Experimental setup	*1:* Blade definition *2:* Axis tilt range	*Pitch:* -17.5° to $+42^\circ$ *rpm:* $550 - 2200$
Commander Propeller [27]	*1:* Torsional stress boundary *2:* Known geometry *3:* Realistic blade (in-service) *4:* Trusted by manufacturers	*1:* Structural properties estimated	*rpm:* $1400 - 1800$ *Pitch:* $26^\circ \ -28^\circ$
SR Blades [28, 29]	*1:* Presented data *2:* Blade configurations *3:* Extensively analysed	*1:* Structural properties *2:* Full boundary	*rpm:* $2000 - 10000$ *Pitch:* $20^\circ \ -50^\circ$ *Scale:* $^1/_8$

Test Case	Summary	Conditions	Date
Smith	Eigenvalue analysis	*rpm:* $5000, 7000, 9000$	1985
[28, 29]	2D strip theory aerodynamics	*Pitch:* $20^\circ \ -50^\circ$	
SR Propellers	Finite element model		
	Conservative results		
Bielawa *et al.*	Eigenvalue & Time-marching	*rpm:* $2000, 8500$	1983
[30]	Gangwani dynamic stall	*Pitch:* 20, 25, 30, 32°	
SR-2 Propeller	Non-linear beam		
	Conservative boundaries		
Reddy and Kaza	Time-marching, modal	*rpm:* $2000, 5000, 8500$	1989
[31]	Gormont dynamic stall	*Pitch:* $30^\circ \ , 50^\circ$	
SR-2 Propeller	Finite element model		
	Conservative results		
Delamore-Sutcliffe	Theodorsen unsteady strip theory	*Pitch:* $0^\circ \ -20^\circ$	2007
[32]	Validated via 2D experiments		
Baker/Hubbard Models	Coupled with rotating beam equations of motion		
	Eigenvalue & Time-marching analysis		
	Deviations from experiment at high pitch angles		
Ognev	Eigenvalue analysis	*rpm:* $500 - 2500$	2011
[33]	Various unsteady inviscid aerodynamic models	*Pitch:* $-20^\circ \ -10^\circ$	
Baker/Hubbard Models	Finite element model		
	Fair agreement to experiments		
Higgins	Time-marching, modal	*rpm:* 1400-1750	2019
[10]	*URANS* and *SAS* CFD	*Pitch:* $27^\circ \ 40'$	
Commander	Non-linear NASTRAN beam		
	Qualitative validation		

Table 2: Summary of propeller stall flutter numerical test cases.

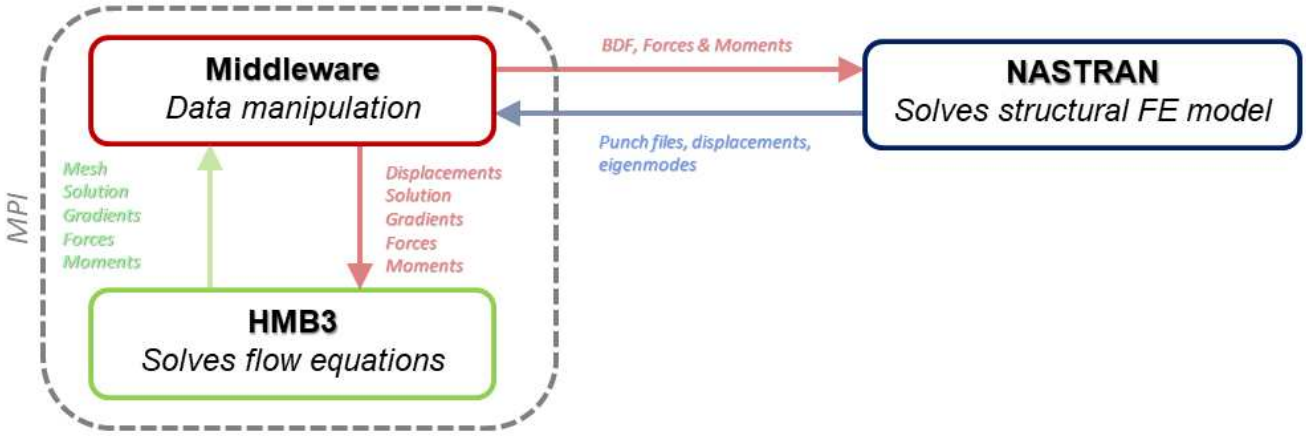

Figure 1: Using Middleware to couple HMB3 to Nastran

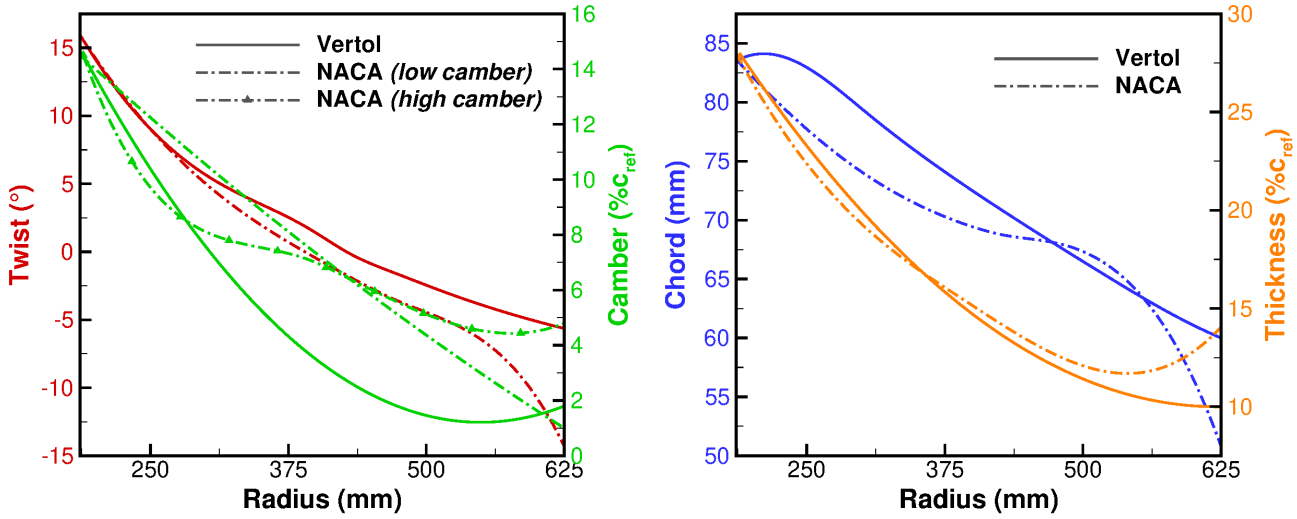

(a) Twist & Camber

(b) Chord & Thickness

Figure 2: Blade Planforms

Table 3: Propeller blade conditions

Number of blades (-)	4
Freestream Velocity (m/s)	38
Propeller Rotational Velocity (rpm)	3000
Reference Chord$_{root}$ (mm)	83.64
Density (kg/m^3)	1.212
Freestream Mach Number (-)	0.11
Freestream Reynolds Number (-)	0.17M
Time-step (°)	0.5
Reduced Frequency (-)	0.346

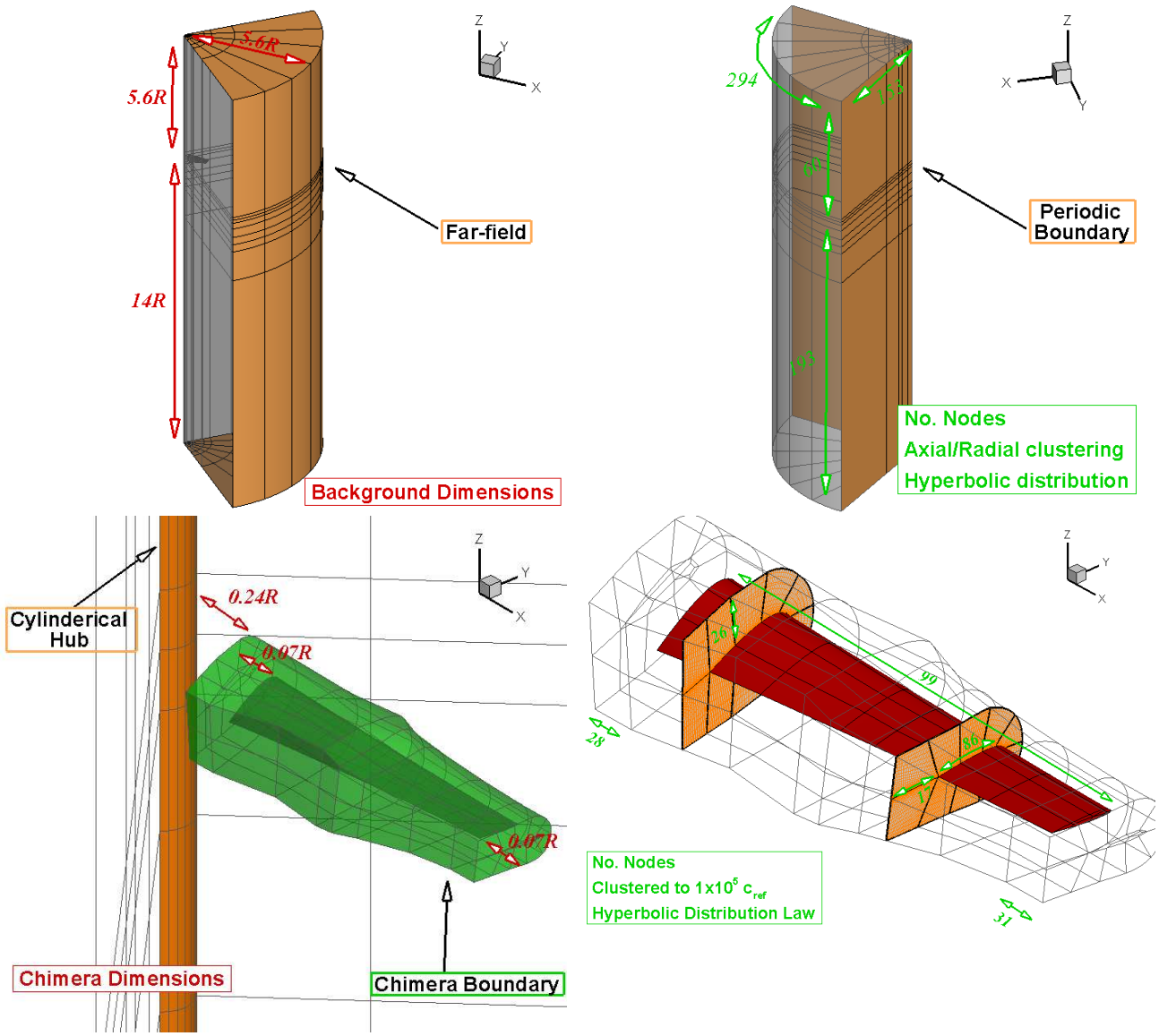

Figure 3: Isolated Blade Grid

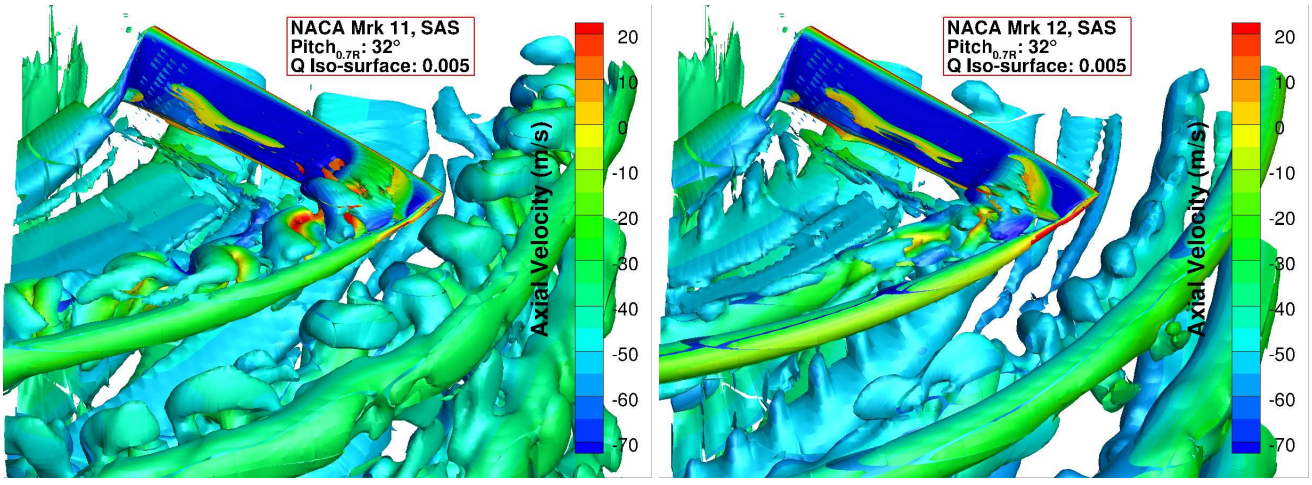

(a) Mrk-11

(b) Mrk-12

Figure 4: Instantaneous iso-surfaces of Q-criteria with value 0.005

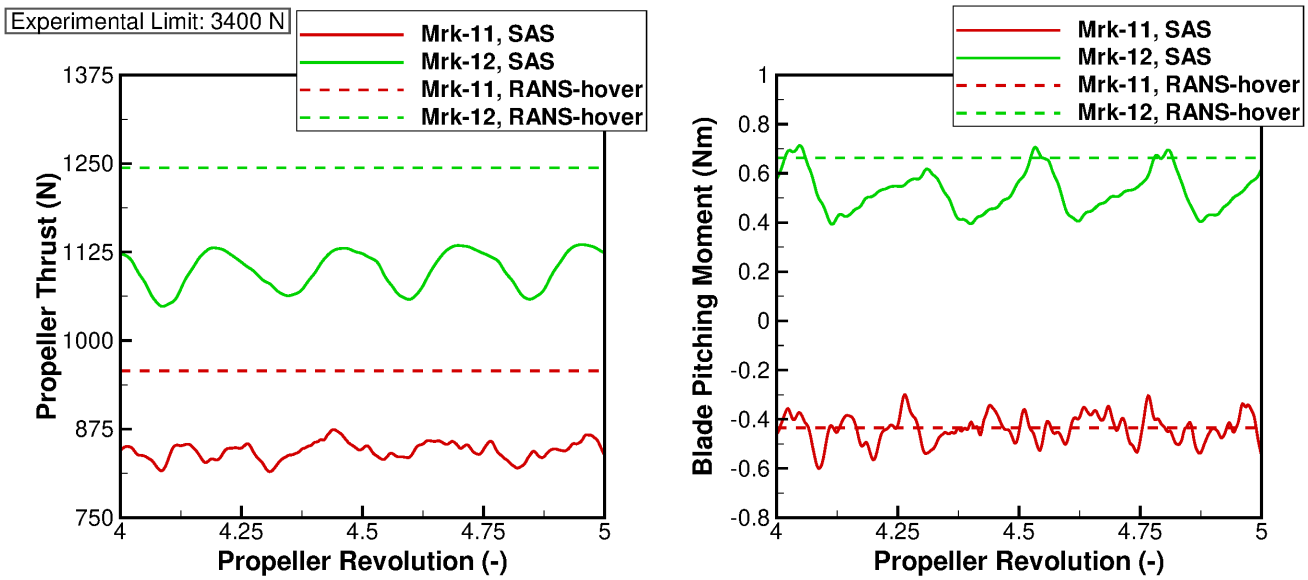

(a) Propeller Thrust

(b) Blade Pitching Moment

Figure 5: Dominant load results for the Mrk-11 and Mrk-12 propeller blades

Table 4: NACA Mrk-11+ structural grids

Part	No. Nodes	No. Elements
Root Fitting	30,018	126,160
Tip Cap	28,299	119,657
Beam Core	12,380	48,817
Rear Filler	33,594	148,738
Aerofoil Skin	83,104	313,581
Beam Skin	54,433	187,269
Total	241,828	944,222

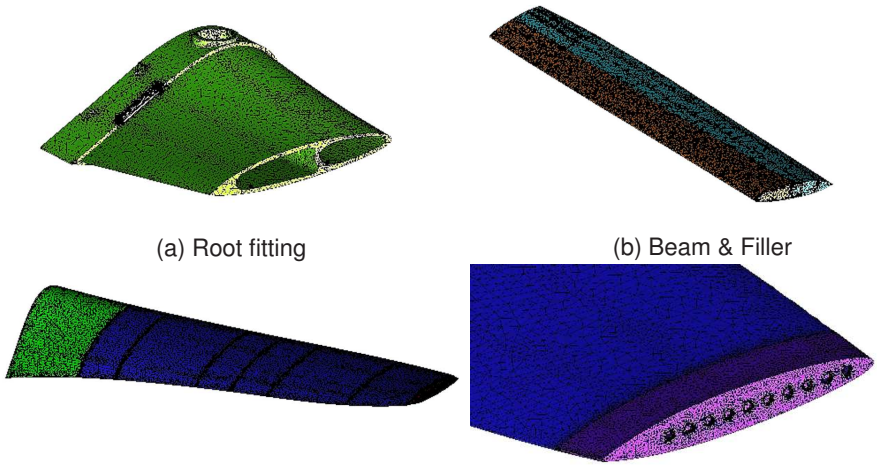

(a) Root fitting

(b) Beam & Filler

(c) Aerofoil skin

(d) Tip-cap

Figure 6: Nastran volume grids for the NACA Mrk-11+

Table 5: NACA Mrk-11+ beam properties

Part	Volume (%Total)
Root Fitting	19.3
Tip Cap	0.4
Beam Core	13.7
Rear Filler	21.6
Aerofoil Skin	37.7
Beam Skin	7.4
Young's Modulus (GPa)	64.15
Poisson's Ratio (-)	0.232
Mass Density (kg/m^3)	1281.2

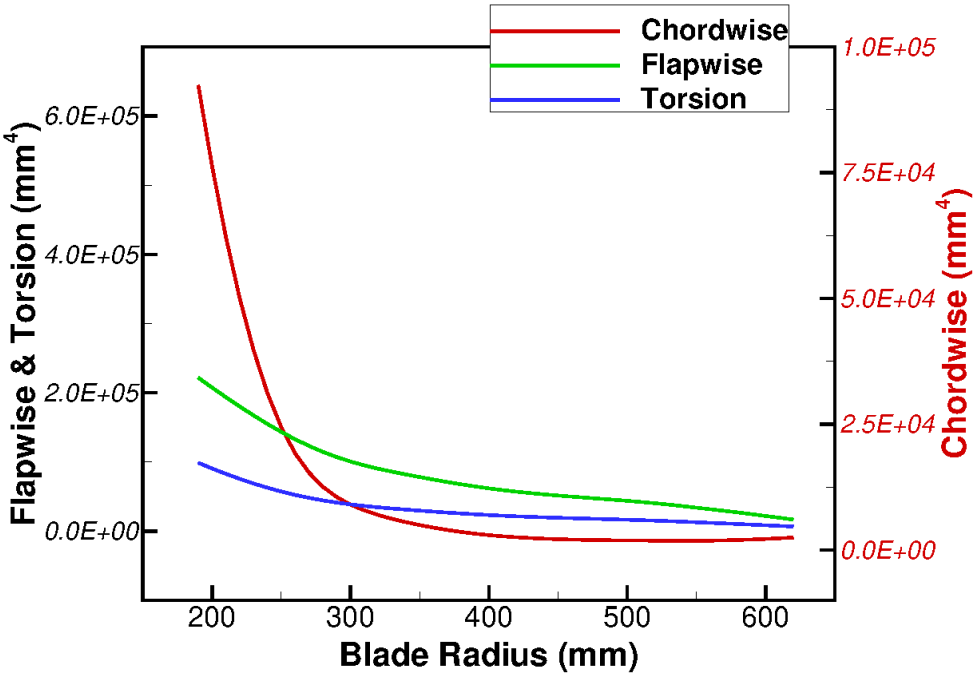

Figure 7: Tuned beam model inertia's for the NACA Mrk-11+

Table 6: Comparison of the non-rotating NACA Mrk-11+ structural models

	Full FEM		**Beam**		
Number	*Shape*	*Frequency (Hz)*	*Shape*	*Frequency (Hz)*	*Δ Frequency (%)*
1	FB	119	FB	121	+1.41
2	LG	398	LG	397	-0.21
3	FB	569	FB	510	-10.41
4	FB	1109	FB	1237	+11.58
5	T	1262	T	1265	+0.18

FB: Flapwise bending, LG: Lag Bending, T: Torsion

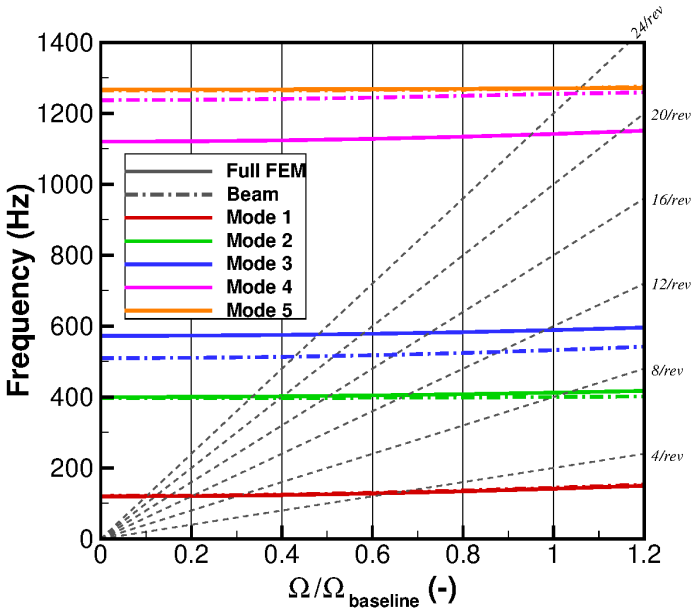

Figure 8: Spoke diagram for the beam and full FEM structural models of the NACA Mrk-11+

Table 7: Supplied modes for the aeroelastic simulations

		Beam
Number	*Shape*	*Frequency (Hz)*
1	FB	114.1
2	LG	400.1
3	FB	532.3
4	FB	1255.0
5	T	1269.9

FB: Flapwise bending, LG: Lag Bending, T: Torsion

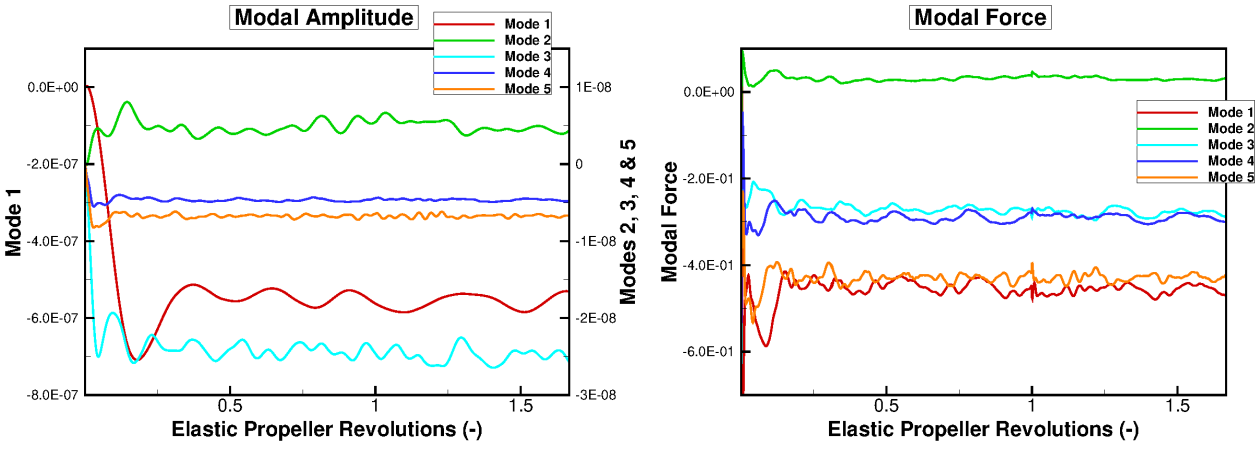

(a) Amplitude

(b) Force

Figure 9: Modal amplitude and force results for the NACA Mrk-11+

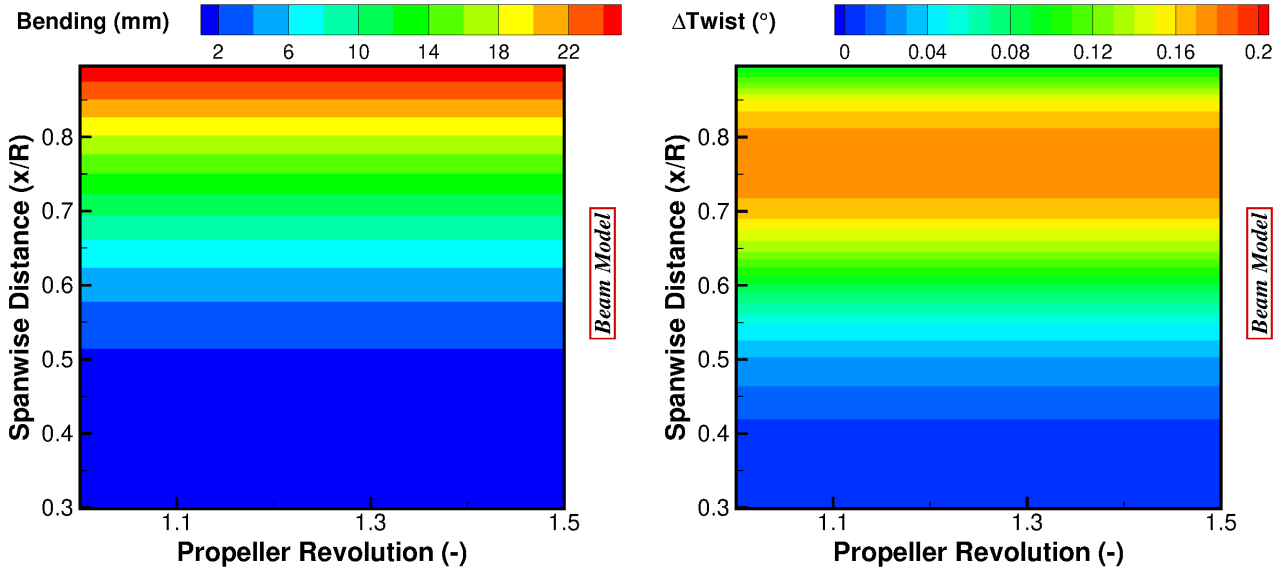

(a) Bending (b) Twist

Figure 10: Blade deformation for the NACA Mrk-11+

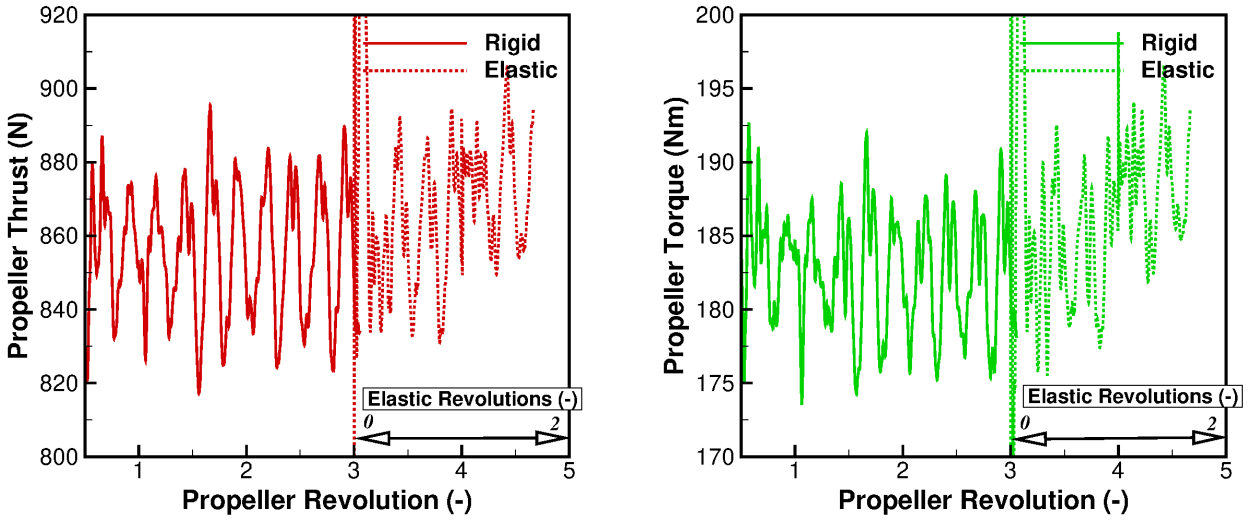

(a) Thrust (b) Torque

Figure 11: Elastic blade loads for the NACA Mrk-11+